Three-dimensional Intravascular Ultrasound Imaging Using a Miniature Helical Ultrasonic Motor

Boquan Wang, Yulin Zhou, Yuchen Wang, Xiaoniu Li, Liyuan He, Zhiyi Wen, Teng Cao, Lei Sun, Dawei Wu, *Member, IEEE*

Abstract—**Existing three-dimensional (3D) intravascular ultrasound (IVUS) systems that combine two electromagnetic (EM) motors to drive catheters are bulky and require considerable efforts to eliminate EM interference (EMI). Herein, we propose a new scanning method to realize 3D IVUS imaging using a helical ultrasonic motor to overcome the aforementioned issues. The ultrasonic motor with compact dimensions (7-mm outer diameter and 30-mm longitudinal length), lightweight (20.5 g), and free of EMI exhibits great application potential in mobile imaging devices. In particular, it can simultaneously perform rotary and linear motions, facilitating precise 3D scanning of an imaging catheter. Experimental results show that the signal-to-noise ratio (SNR) of raw images obtained using the ultrasonic motor is 5.3 dB better than that of an EM motor. Moreover, the proposed imaging device exhibits the maximum rotary speed of 12.3 revolutions per second and the positioning accuracy of 2.6 μm at a driving voltage of 240 V_{P-p}. 3D wire phantom imaging and 3D tube phantom imaging are performed to evaluate the performance of the imaging device. Finally, the *in vitro* imaging of a porcine coronary artery demonstrates that the layered architecture of the vessel can be precisely identified while significantly increasing the SNR of the raw images.**

Index Terms—**Intravascular ultrasound imaging, ultrasonic motor, high-frequency transducer, mechanical scanning device.**

I. INTRODUCTION

CARDIOVASCULAR diseases (CVDs) are among the main causes of health deterioration in many regions around the world. Nearly four-fifths of global CVD fatalities occur in resource-limited areas [1–4]. Considering the number of CVD fatalities, we are facing a severe public health problem; hence, precisely identifying these diseases is essential for guiding therapeutic strategies [5]. Three-dimensional (3D) intravascular ultrasound (IVUS) systems are essential for the tomographic assessment of vessel and plaque components, dimensions, and distributions [6]. They aid our understanding of the detailed assessment of the influence of geometric (e.g., diameter and curvature) [7, 8] and hemodynamic (e.g., shear stress, compressive stress, and tensile stress) [9] factors on atherogenesis and plaque progression. Generally, 3D IVUS imaging is performed using two methods [10–12]. The first type involves scanning a target using motors to rotate and pullback a single-element ultrasonic transducer. The second type involves the pullback of a ring array transducer to capture 3D ultrasonic images (e.g., the Eagle Eye Platinum catheter manufactured by Philips Corporation). Nevertheless, with sparse ultrasonic transducer elements inside the catheter, the side lobes become a critical concern, reducing the transverse resolution. To increase the number of elements, slicing smaller elements is essential, making it difficult to guarantee consistently high performance of each element [13]. The single-element scanning method does not have the aforementioned problems and remains its own advantages (e.g., low cost, excellent near-field resolution) in clinical applications [14].

Inspired by the IVUS single-element scanning method, researchers have advanced the IVUS imaging performance and developed multimode imaging systems for the improved characterization of CVDs. For instance, in IVUS, superharmonic images obtained at higher harmonics (third or higher harmonics) achieve a higher tissue contrast than ultrasonic images produced using second-order harmonics or fundamental frequencies [15]. Micromachined 1–3 composite ultrasonic transducers can realize wider bandwidths, which significantly reduce the pulse length of the transmitted wave and helps IVUS perform high-resolution imaging of tiny vessels [16]. Additionally, the integrated IVUS and intravascular optical coherence tomography (IV-OCT) imaging system facilitates high-resolution OCT for the precise identification of thin fibrous caps, whereas IVUS can visualize

Boquan Wang, Yuchen Wang, Xiaoniu Li, Liyuan He, Zhiyi Wen, Teng Cao, and Dawei Wu are with the State Key Lab of Mechanics and Control of Mechanical Structures, Nanjing University of Aeronautics and Astronautics, Nanjing 210016, Jiangsu, China (*Corresponding author: Dawei Wu, dwu@nuaa.edu.cn).

Yulin Zhou is with the Medical College of Soochow University, Suzhou 215006, Jiangsu, China, and also with the Department of Urology, Jinling Hospital, Medical School of Nanjing University, Nanjing 210005, Jiangsu, China. (Boquan Wang and Yulin Zhou are co-first authors).

Lei Sun is with the Interdisciplinary Division of Biomedical Engineering, The Hong Kong Polytechnic University, Hong Kong SAR, China.

the overall volume of plaques [17, 18]. Furthermore, the integrated IVUS and near-infrared spectroscopic imaging system and the IVUS and intravascular photoacoustic (IVPA) imaging system can characterize the lipid composition of plaques [19–22]. The integrated IVUS and fluorescence system delineates the morphological features of atherosclerotic plaques and characterizes the molecular specificity of their compositions [23]. All these catheter-based single-element scanning systems follow the same principle for 3D intravascular imaging; the imaging catheter is actuated by combining rotary and linear electromagnetic (EM) motors. Concurrently, EM interference (EMI) induced by EM motors frequently occurs during data acquisition. The solutions to this issue include the EM shielding of the system hardware, multiple scanning at the same position, and averaging procedure to reduce the background noise and improve the signal-to-noise ratio (SNR) of the raw image [24]. However, the cumbersome EM shielding methods increase the system cost and repeated scanning reduces the temporal resolution of 3D imaging. Besides, current IVUS systems incorporate bulky drive mechanisms that are challenging to miniaturize. Lightweight systems will be easier to handle and more advantageous in transportation [25]. Consequently, raw image SNR improvement and miniature system development are essential to complement the current catheter-based modalities for enhancing diagnostic accessibility.

Ultrasonic motors are considered excellent candidates for IVUS motors, as they do not induce EMI and their output efficiency is independent of size. Moreover, they are effective actuators that deliver high position resolutions and fast responses [26–30]. The concept of ultrasonic motors for IVUS applications was reported in 2006. Tanabe et al. produced a miniature ultrasonic motor using a helical coil as the stator [31]. The B-mode ultrasonic image of an aluminum plate was obtained by scanning the ultrasonic transducer driven by the acoustic waveguide. In 2011, Chang et al. confirmed the practicability of using ultrasonic motors for intravascular OCT. They eliminated insertion losses caused by optical coupling elements and many optical interfaces [32]. Notably, their system relies on a motor to rotate the mirror for scanning, which is limited to scanning a single cross-section. Relying solely on a rotary ultrasonic motor fails to achieve 3D intravascular imaging. Thus, the development of EMI-free, lightweight, and miniature 3D scanning devices is urgently needed for emerging IVUS applications.

To further the previous studies, in this paper, the IVUS catheter was driven using a miniature helical ultrasonic motor to achieve high-resolution 3D ultrasonic images of the coronary arteries (inner diameter = ~2 mm). Using the ultrasonic motor, complicated EMI-shielding work can be avoided to reduce system costs. The miniature IVUS scanner can significantly simplify the final assembly of IVUS mechanical systems and provides a potential for future integration into mobile imaging devices. 3D wire phantom, 3D tube phantom, and *in vitro* porcine coronary artery imaging were performed to evaluate the performance of the proposed imaging device.

II. METHODS

A. Ultrasonic Motor Design

The motor comprises five assembly parts: a hollow screw as the rotor, four lead zirconate titanate (PZT) sheets, a rectangular phosphor bronze body with internal threads as the stator, a pre-pressure device consisting of a nut and spring, and insulated plastic housing.

The motor was fabricated using the following process. First, each PZT sheet (thickness: 1 mm, length: 30 mm) was bonded to the phosphor bronze body (outer diameter: 5 mm, inner diameter: 3 mm, length: 30 mm). The mutually symmetrical PZT sheets on the metal body exhibited the same polarization direction to excite the first-order bending vibration mode. Second, the rotor (outer diameter: 2.95 mm, inner diameter: 1 mm, pitch: 0.35 mm, length: 95 mm) was passed through the nut, spring, and phosphor bronze body. The pre-pressure was generated by squeezing the spring using the nut. These components were embedded in the 3D printed plastic housing to ensure that they were coaxial and stationary. After the assembly, the weight of the motor was 20.5 g.

The helical ultrasonic motor operates in a friction drive mechanism; thus, the pre-pressure between the stator and rotor is essential for optimizing the output. A key assembly step in the fabrication process is the pre-pressure device. First, a 3D-printed plastic shell was used to insulate the surface of the motor and ensure that the stator, rotor, nut, and spring were coaxial. Next, a nut and stator squeezed the spring to provide pre-pressure in the axial direction of the motor. Then, the nut was rotated to adjust the tension of the spring. The applied pre-pressure was calculated by dividing the measured force by the contact area (6.12 mm^2) between the spring and the stator. The greater the compression deformation of the spring, the greater the pre-pressure (maximum pre-pressure: 0.052 N/mm^2) generated on the threaded surface between the stator and the rotor. Consequently, the greater the output torque of the motor. The maximum torque of the motor at a voltage of 200 $V_{p–p}$ and a pre-pressure of 0.052 N/mm^2 was measured to be ~182 mN·m using the balance force method.

B. Driving Principle

Fig. 1 shows the driving principle of the helical ultrasonic motor. First, two AC signals are input with the same driving frequency and amplitude and a phase difference of 90° in the two sets of orthogonal piezoelectric plates to induce two bending modes (Fig. 1(a)). Second, the combination of two vertical bending vibrations can induce the elliptical motion of the stator particles [33]. Fig. 1(b) shows a motion analysis of point � (red ellipse) on the stator surface, which can be decomposed into two trajectories of the elliptic motion: � (blue ellipse) and (green ellipse). The black dotted lines represent the equilibrium position of the stator, and the solid black lines represent the stator position at time .

To improve the driving efficiency of the motor, the contact area between the stator and rotor can be increased using processing threads in the stator. Owing to the threading

connection, the rotor starts to pull back while rotating and produces a helical motion. The catheter is coaxially connected with the rotor. Thus, the catheter can realize helical scanning along with the rotor.

Fig. 1. Driving principle of the ultrasonic motor. (a) Vibration mode of the
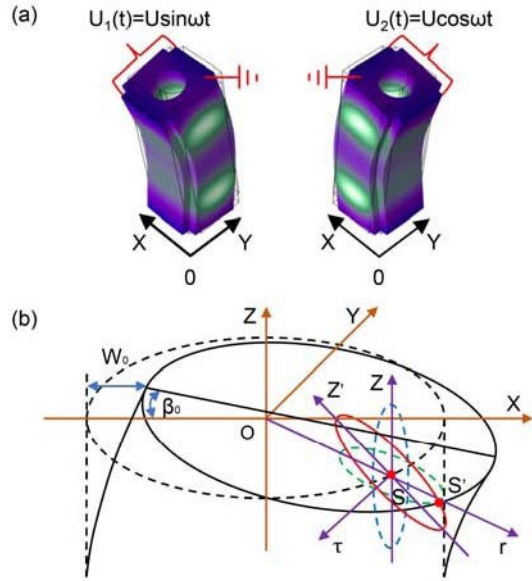
stator. (b) The elliptic trajectory of point S at the stator.

C. Device Construction

Fig. 2(a) shows an image of the IVUS device, which comprises an IVUS catheter and helical ultrasonic motor. First, a single-element transducer (Blatek Inc., USA) with dimensions of 0.6-mm length, 0.5-mm width, 0.2-mm thickness, and a center frequency of 41.9 MHz is mounted on a metal tube with outer and inner diameters of 0.7 and 0.5 mm, respectively. Second, the metal tube is inserted in the torque coil (outer diameter: 0.9 mm). The coil is crucial for the effective transmission of the torque. Finally, the 60-mm-length catheter is inserted in the hollow rotor of the motor to ensure the coaxiality of the rotating parts (Fig. 2(b)). Fig. 2(c) shows the components of the helical ultrasonic motor.
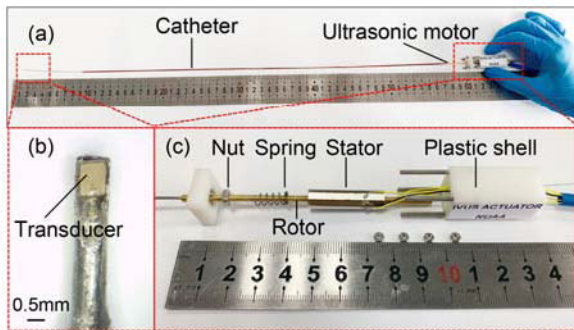

Fig. 2. Image of the intravascular ultrasound device. (a) Main components of the device. (b) A high-frequency transducer sticks on the catheter tip. (c) The proposed hand-held helical ultrasonic motor.

D. Imaging System Design

The imaging system involving mechanical transmission, ultrasound transmission, and imaging reconstruction. For

ultrasound transmission, and imaging reconstruction. For mechanical transmission, sinusoidal and cosinusoidal signals with equal amplitude (1 V_{P-p}) and frequency (21.48 kHz) and a phase difference of 90° were generated using a function generator (AFG1062, Tektronix Inc., USA). Then, a power amplifier (75A250A, Amplifier Research Inc., USA) was used to amplify these signals to 80 V_{P-p}, which excited the motor driving the IVUS catheter. For ultrasound transmission, the electrical signals (1 cycle sinusoidal pulse at 41.5 MHz with a pulse repetition frequency of 2500 Hz) were transmitted from the Verasonics Vantage 64LE high-frequency ultrasound system (Verasonics Inc., USA) to the single-element transducer when a synchronized trigger was obtained from the function generator [34]. Then, the same ultrasound system recorded the digitized ultrasound signals, eventually stored in a computer. During the acquisition of high-frequency ultrasound signals, the 4/3 sampling method in conjunction with the anti-alias filter was used to acquire signals with frequencies above the 2/3 center frequency of the transducer (27.9 MHz). First, a 31-MHz high-pass filter is required to eliminate any low-frequency signal that could be added to the desired signal after aliasing. After that, a 50-MHz low-pass filter is required to limit out-ofband high-frequency noise [35]. Finally, the signal was inverted and triple shifted to the original frequency band and the accurate high-frequency ultrasonic echo signal was acquired. For imaging reconstruction, the collected signals were filtered using bandpass filters (bandwidth: 20–60 MHz) and the Hilbert transform was then performed. The images were then converted to polar coordinates for display.

E. Imaging Evaluation

Three ultrasonic phantoms, namely, tungsten wire phantoms A and B and an agarose tube phantom, were produced for image evaluation. The transducer is excited by a pulser-receiver (5073PR, Olympus, Japan) with a repetition frequency of 1 kHz, 1 μJ pulse energy, 39 dB receive gain and 50 Ω damping factors. The bandwidth of the transducer was evaluated using the pulse-echo response. The porcine coronary artery was used for *in vitro* imaging evaluation.

The wire phantom A comprises five parallel tungsten wires with a diameter of 10 μm each, following a trapezoidal arrangement. The imaging catheter scans wire phantom A vertically to measure the transverse and axial resolution of the system.

Tungsten phantom B consists of five tungsten wires with a diameter of 10 μm each (Fig. 3(a)), mounted in a hollow cylinder whose distance the catheter center was between 2 and 6 mm. It was used to verify the distribution around the imaging catheter and enable accurate angular imaging. The catheter was inserted into the center of the tungsten wire phantom, and helical scanning was performed in water. To obtain comprehensive information on the tungsten wires, the Aline was sampled at 649 points with a corresponding depth of 8 mm.

The agarose tube phantom (Biowest agarose, Gene Company, Spain), comprising three polyethylene (PE) tubes (diameter of 2 mm) in a nylon shell (inner diameter of 7 mm) fixed with 3%

agar and 30% evaporated milk (Fig. 3(b)). These tubes were distributed around agarose at 120° intervals at radial positions of 3, 4, and 5 mm.

To demonstrate the clinical applications of the IVUS system, *in vitro* imaging using the hand-held IVUS scanning device was performed in a porcine coronary artery (inner diameter = ~2 mm) after soaking in alcohol (Fig. 3(c)). To obtain sufficient support for pushing the IVUS catheter forward, we introduced a guidewire with a 0.2-mm diameter, comparable in size to the IVUS guidewire (Confianza-12g, Asahi Intecc, Japan) used in clinics. We straighten the guide wire in advance to support the isolated vessel and insert the catheter with a protective tube along the wire into the vessel for scanning; the wire also serves as a locator during the imaging process. Therefore, 40 cross-sectional ultrasonic images were sequentially acquired using 10-rps rotary speed and 400 A-lines per B-mode image.

Since the 3D scanning system lacks the slip ring, the wire of the transducer remains 70 cm long after passing through the rotor to avoid probe damage due to knotted wire after pulling back 95 mm.

Fig. 3. Phantoms and the porcine coronary artery for evaluating the proposed system. The diagram shows the design of the circular wire phantom comprising
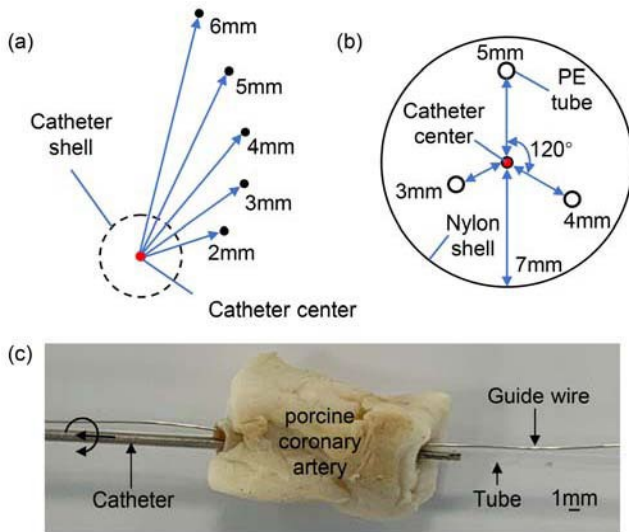
five tungsten wires (diameter of 10 μm), respectively, and (b) agarose tube phantom with three PE tubes (diameter of 2 mm) and a nylon shell (inner diameter of 7 mm). The radius from the tubes to the center increased from 3 to 5 mm. (c) Image of the experimental setup for porcine coronary artery imaging.

F. Motor Evaluation

In addition to a limited size range, an IVUS catheter requires stable rotation and a high-speed ultrasonic motor. The basic performance characterization of a motor, such as vibration, maximum speed, optimal working distance, rotary uniformity, positioning accuracy, and SNR competition, must be tested first before the imaging evaluation. Our proposed helical ultrasonic motor design was partially shown in a conference proceeding [34]; however, the system performance was not previously described and the conducted *in vitro* experiments were primitive. Fig. 4 shows a performance test of the ultrasonic motor.

The frequencies of the two first-order bending modes were measured using a laser Doppler vibrometer (PSV-500F-B, Polytec Inc., Germany). The maximum rotor speed and the optimal working distance could be observed using the laser velocimeter.

As the catheter was pulled back, the positioning accuracy of rotor was measured using a laser displacement sensor (LK-H150, Keyence Inc., USA). Dual modulated signals were input to the motor at a driving voltage of 240 V_{p-p}. The interval of each signal was 200 ms, and the AC signals accounted for 20 ms.

The rotary uniformity of the motor was verified at a pre-pressure of 0.016 N/mm^2 and a voltage of 140 V_{p-p}. When the rotor speed was measured, the sensor sampling rate was set to 20 kSa/s. We converted the speed results into an angular error. In theory, at 10 rps, the change in angle was 9° per 2.5 ms.

To accurately compare the SNR of the obtained images with those of the two motor types (the setup is shown in Fig. 4(f)), the catheter was passed through the motor and not fixed to the rotor; hence, it did not rotate with the rotor. The stationary transducer emitted ultrasound waves to an iron block with dimensions of 50-mm length, 30-mm width, and 10-mm thickness. The SNR was calculated as follows [36, 37]:

$$\lozenge \ 20(\,$$

$$)_{,\,} (1)$$

where $\lozenge$ and $\lozenge$ represent the mean values of the iron signal and background noise after the standard deviation, respectively.

III. RESULTS

A. Experiment to Evaluate the Motor Performance

Results show that the frequencies of the two first-order bending modes were 21.53 and 21.45 kHz, respectively, and the frequency difference between the two bending modes was 80 Hz (Fig. 4(a)). Errors in the processing and assembly steps were the main reason for the frequency difference. The intersection of the two-phase modal frequencies (21.5 kHz) was used as the drive signal frequency to ensure that the two modalities with the same amplitude can excite a pure traveling wave. Based on the previous empirical determination of ultrasonic motor two-phase modal frequency consistency adjustment [38], the frequency difference of 80 Hz accounted for 0.37% of the driving frequency, which is negligible in motor driving performance.

In Fig. 4(b), each driving voltage corresponded to an average speed. When the pre-pressure was 0.016 N/mm^2, a maximum speed of 12.3 rps was reached, with a voltage of 240 V_{p-p}. The red line shows the rotor speed variation in the displacement interval from 5 to 95 mm at a voltage of 200 V_{p-p}. The maximum rotary speed was up to 11.3 rps at 40 mm of the linear rotor movement. In the displacement interval of 30–70 mm, the motor speed was approximately 80% of the maximum speed. Therefore, this optimal working distance range guaranteed stable 3D imaging.

Fig. 4(c) shows the axial displacements of the rotor for 18 cycles. The average positioning accuracy of the motor was 2.6 µm. In Fig. 4(d), the measurement results showed that the maximum angular variation of 12.8° or 5.5° was achieved every
2.5 ms at 10 rps with an angular error of 3.8°. In Peng's study [13], the maximum angular variation of the micromotor was 4° every 2.5 ms at 10 rps. At an identical rotary speed of 10 rps, the angular error of the helical ultrasonic motor was smaller than that of the EM motor.

The transducer captured 800 Aline signals with an imaging depth of 10 mm and the iron block imaging results are shown in Fig. 4(e and f). The SNR values of raw images obtained using the ultrasonic and EM motors were 41.2 and 35.9 dB, respectively, and the SNR of the ultrasonic motor was 5.3 dB higher than that of the EM motor.

Fig. 4. Performance testing of the proposed motor. (a) Frequency response of
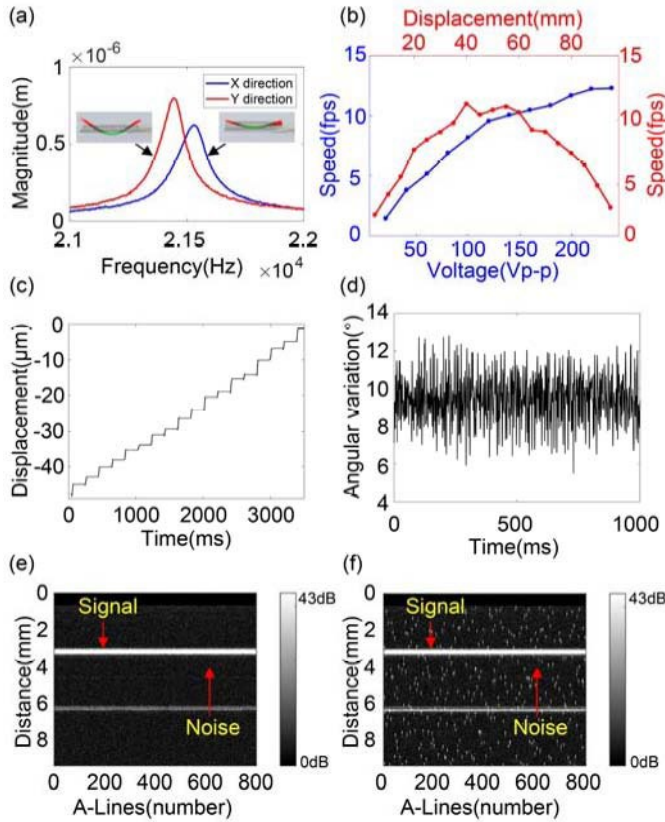

the stator. (b) Average speed at different driving voltages and different linear displacements. (c) Angular error at a driving voltage of 140 V_{P-P} and a pre-pressure of 0.016 N/mm^2. (d) Measurement results of the motor positioning accuracy in 18 cycles. Ultrasonic B-mode images were obtained using the (e) ultrasonic motor and (f) electromagnetic motor.

B. Transducer Evaluation

The resolution of the IVUS system was measured using the image of a tungsten wire with a 10-µm diameter. Fig. 5(a) shows the ultrasonic images of the tungsten wire at different depths. Fig. 5(b) presents an enlarged view of the dashed box in Fig. 5(a), with the tungsten wire located at a depth of 2.1 mm. From the tungsten ultrasonic image, the maximal amplitude of the signal points is indexed and transverse and longitudinal dashed lines are plotted through this point.
In Fig. 5(c and d), the points represent the transverse and axial

experimental data corresponding to the dashed lines in Fig. 5(b), respectively. The data are fitted using a Gaussian function to estimate the spatial resolution in both directions. We measured the full width at half maximum (FWHM) [39] and obtained transverse and axial resolutions of 371 and 48 µm, respectively. To ensure that no information was missed during the 3D scanning process, the thread pitch of the motor was manufactured at a pitch of 350 µm, which was smaller than the transverse resolution of the system. Fig. 5(e) demonstrates the quantitative analysis of the axial and transverse resolutions of the ultrasound system at different imaging depths.

Fig. 5. Performance testing of the ultrasonic transducer. (a) B-mode image of the tungsten wire with a diameter of 10 µm at different depths. (b) Enlarged view of the dashed box in (a). (c) Transverse and (d) axial resolutions of the
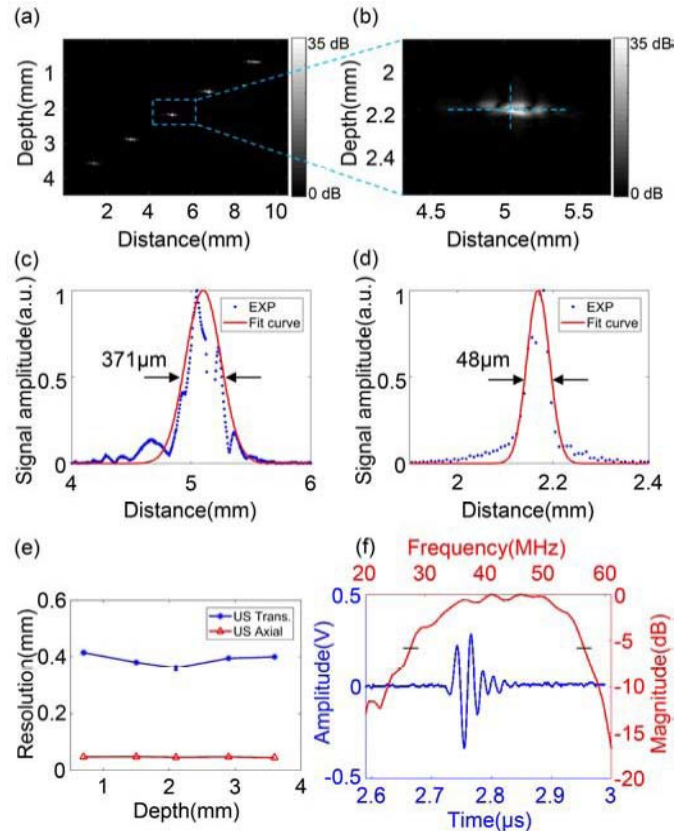
intravascular ultrasound system at 2.1-mm depth. (e) Resolution of the ultrasonic image at different depths. (f) Measured pulse-echo response (blue solid line) and frequency spectrum (red solid line) of the transducer.

The pulse-echo response of the transducer was measured to evaluate the performance of the transducer. A quartz reflector was placed 2.1 mm from the transducer, which corresponds to the distance of its focal length. The transducer was excited using a pulser-receiver. The center frequency of the transducer and −6 dB bandwidth were 41.9 MHz and 69%, respectively, which were observed in the pulse-echo test (Fig. 5(f)).

C. Phantom Imaging Evaluation

The B-mode image (Fig. 6(a)) shows that the five tungsten wires were located at 2.08, 3.26, 4.00, 5.00, and 5.94 mm. The 3D images comprising 15 cross-sectional ultrasonic images

(Fig. 6(c)) were measured by pulling back the catheter at a distance of 5.25 mm, and the dynamic range of the images was set to 35 dB.

Fig. 6(b) shows a reconstructed B-mode image of the agar phantom with a nylon shell and three PE tubes. The tube phantom was submerged in water. The tube edge was not detected at a distance of 5 mm from the center because the ultrasonic beam scattering of the agar phantom and the reflection of the ultrasonic beam from the edge of the tube were beyond the detection area of the transducer. For reference, the amplitude of the water echo signal was normalized to 0 dB before phantom imaging and each dynamic range of the B-mode image was set to 40 dB. Fig. 6(d) shows the 3D tube phantom image with a diameter of 16 mm (radial imaging depth of 8 mm) and a longitudinal length of 5.25 mm.
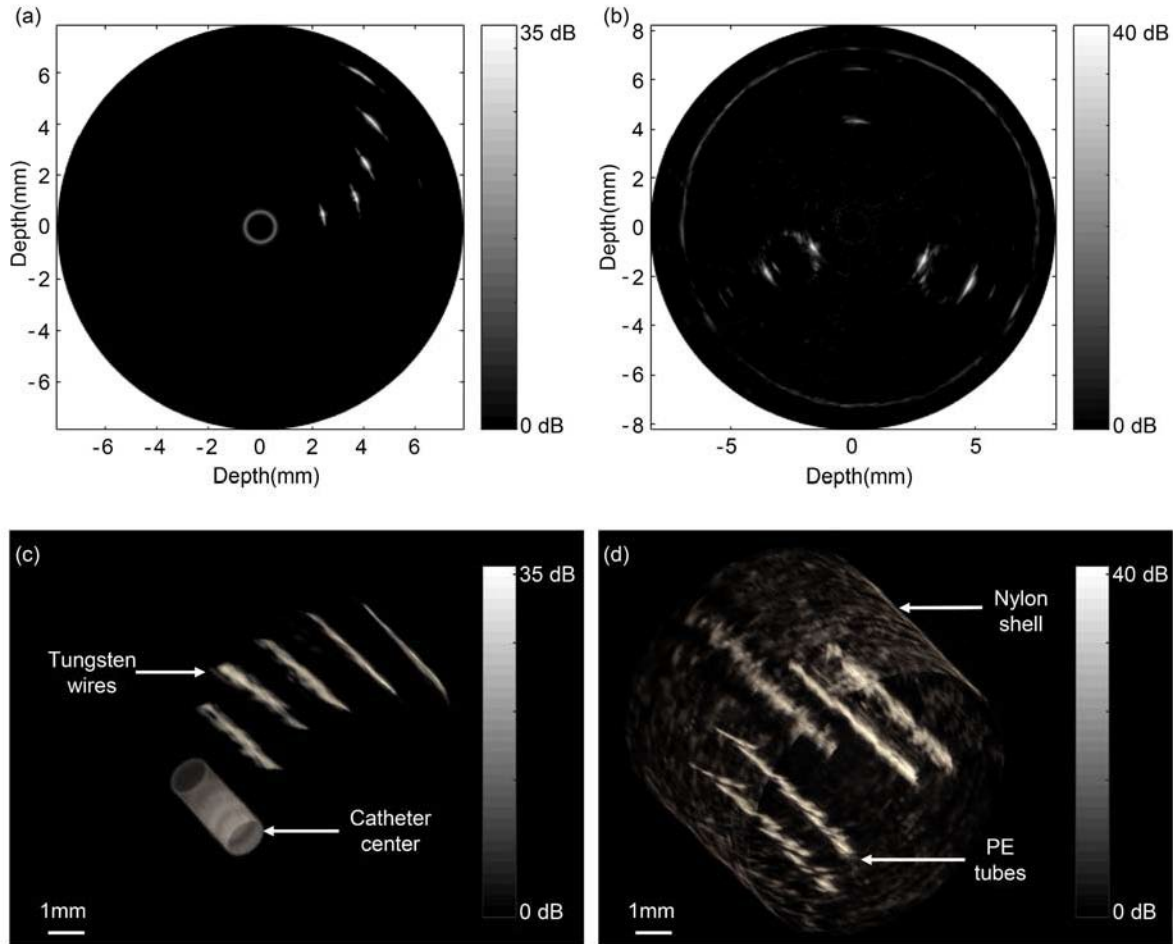

Fig. 6. Ultrasonic image reconstruction of the circular tungsten wire phantom and agarose tube phantom. B-mode images of the (a) tungsten wire phantom and (b) agarose tube phantom with dynamic ranges of 35 and 40 dB, respectively. 3D images of the (c) tungsten wire phantom and (d) agarose tube phantom.

D.   In Vitro Imaging of the Porcine Coronary Artery The porcine coronary artery was used for *in vitro* imaging evaluation. Additionally, an intravascular ultrasound imaging system with the EM motors as the driving source was established and served as a reference for imaging experiments. We compared the raw ultrasonic images obtained using two types of motor drives at the same rotary speed. The cross-sectional scanning of the porcine coronary artery was performed using two types of motors, and the obtained images are shown in Fig. 7(a and b). Comparing the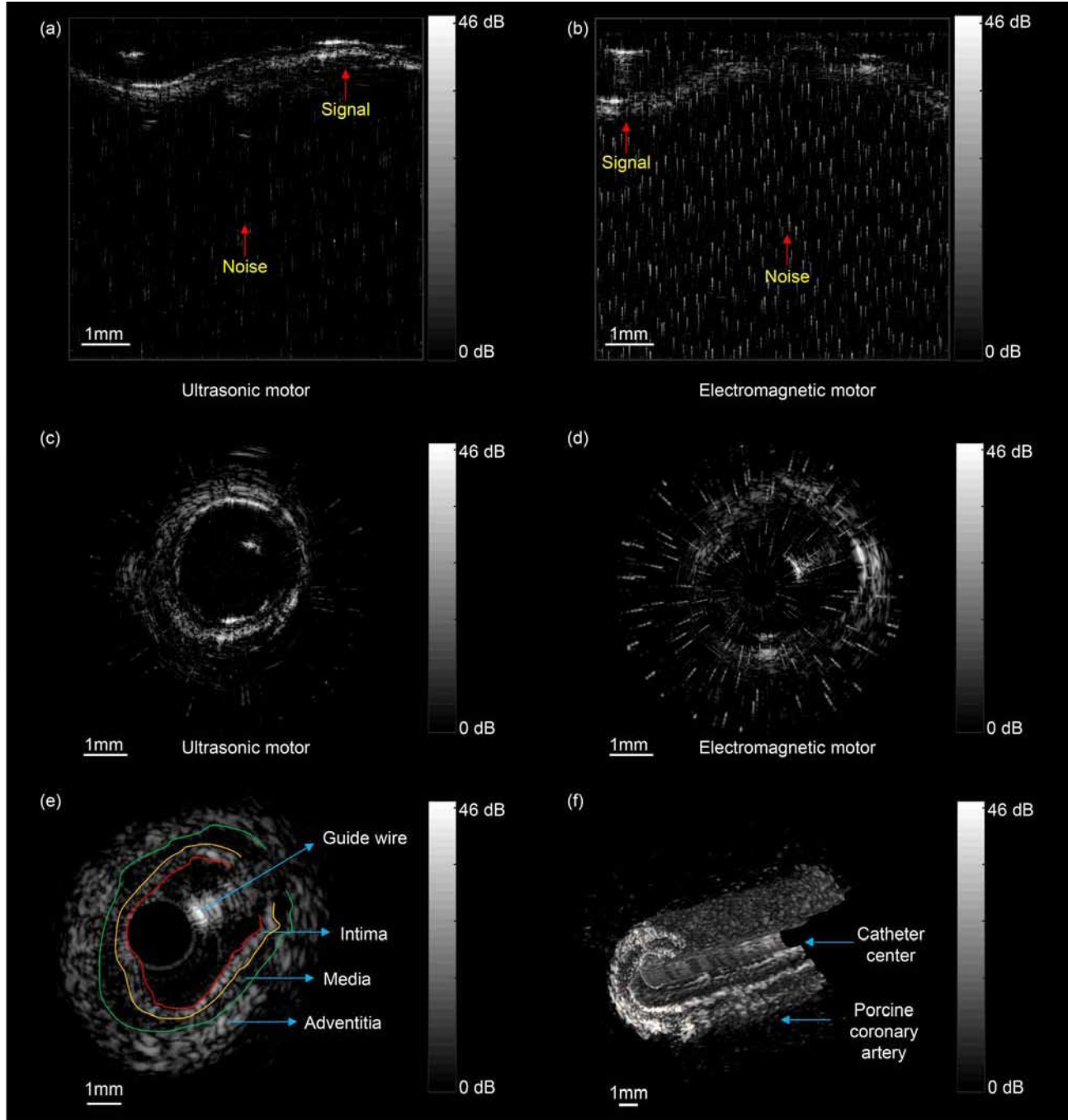 SNR of the two images, based on Equation 1, ◊ and ◊ denote the mean value of the vascular signal and the standard deviation of the background noise, respectively. The calculated values of SNR in Fig. 7(a and b) were 45.3 and 37.8 dB, respectively, while the SNR of the raw images obtained using ultrasonic motor significantly improved. Fig. 7(c and d) shows the polar coordinate transformation after interpolation of (a and b), respectively. The background noise in the raw images obtained using the ultrasound motor was predominantly caused by the surrounding electromagnetic environment.

As observed in the B-mode image (Fig. 7(e)), the intima, medial, and adventitia of blood vessels could be identified using the boundary demarcated by the strength signal, represented by red, yellow, and green lines, respectively. The image is displayed with a dynamic range of 46 dB. We removed the artifacts from the guidewire and constructed a 3D ultrasonic image of the Porcine coronary artery with 0°–310° angles and 14-mm length. Fig. 7(f) shows the morphology of the vessel.

IV. Discussion

Herein, a mechanical scanning method incorporating a helical ultrasonic motor was designed to explore the potential of 3D IVUS imaging. With the integration of the helical ultrasonic motor, which exhibits a compact structure and is free of EMI, the IVUS system could obtain precise 3D images. Without cumbersome denoising procedures, the raw images obtained using the ultrasonic motor showed better SNR than those obtained using EM motors. Moreover, the helical ultrasonic motor showed a compact and self-locking structure without a decelerating mechanism in power failure and its size was considerably smaller than the size of traditional EM motors, which was useful in the miniaturized design of imaging systems. These features exhibit the promising potential for the use of IVUS systems at the point of care as clinical decision support tools in the health care systems of resource-poor regions.

Fig. 7. Ultrasonic images of the *in vitro* porcine coronary artery. Raw B-mode images obtained using the (a) ultrasonic motor and (b) electromagnetic motor. (c and d) Polar coordinate transformation images of (a and b), respectively. (e) The layered architecture of the vessel identified using the boundary demarcated by the strength signal (f) 3D ultrasonic images of the vessel acquired *in vitro* over a 14-mm range with a covering angle of ~310°.

The application of the helical ultrasonic motor for 3D IVUS imaging, while exciting, requires further exploration. Because the current system lacks the slip ring, prolonged motor rotation causes the cable to knot. One approach to address the above concerns is taking advantage of the conductive properties of sodium sulfide solution in conjunction with miniature conductive bearings, which can effectively avoid damage to the transducer from knotting the cable [40]. In addition, the

imaging distance depends on the length of the threaded rotor. The maximum imaging distance of our motor was 95 mm, and the optimal working distance was 40 mm, limiting its potential in long-distance scanning applications. Another disadvantage of the motor is its complex fabrication owing to high-precision threads. To completely capture 3D information, the pitch length of spiral scanning must be less than the transverse resolution of the system; hence, the machining accuracy of the pitch limits the improvement in the transverse resolution. A new type of flexible ultrasonic motor without threads has been proposed to address these issues, which is expected to drive the catheter for helical motion [41]. The resolution and scanning distance of the system is no longer limited by the thread accuracy and length of the conventional rotor. The novel motor combined with an appealing anti-knotting approach [40] for wires is promising for long-distance scanning imaging.

The imaging speed of 25 frames per second has been shown to achieve real-time display mode during *in vivo* intravascular imaging [42]. When a proximal motor drives the catheter via the tortuous vessel, the current maximum speed of the catheter is further hindered by the friction between the catheter coil and the vessel wall [43, 44], which is insufficient for *in vivo* applications. To increase the imaging speed further, the PZT with a higher mechanical factor and lower dielectric loss than the PZT8 can be selected as the excitation source of the motor. The high-quality stator processing and assembly accuracy contribute to an increased coupling efficiency of the two-phase modal and adds friction-decreasing materials (e.g., grease) at the stator–rotor contact interface to reduce the impact of frictional heat generation on the PZT performance.

Since the 4/3 sampling method limits the passband to a relative bandwidth of 67% and the cutoff frequency of the anti-alias filter is limited to the highest setting of 50 MHz, resulting in missing signals below 31.25 MHz and above 50 MHz in the image [35]. One solution would be to use an acquisition card with larger bandwidth and sufficient sampling rate to completely capture the high-frequency signal.

To achieve a broader range of potential intravascular imaging applications for future research, a miniature flexible ultrasonic motor that can be integrated into the distal end of the catheter is the key to accurate imaging and reduced medical costs. The miniature motor-driven micromirror is beneficial for increasing the scanning speed of the system. Moreover, the hollow ultrasonic motor can simultaneously integrate coaxial cables and optical fibers, which can be used to develop a new multimodal intravascular photoacoustic and ultrasound imaging device. Further, magnetic ultrasound is expected to be combined with IVUS to identify macrophages as the markers of inflammation [45]. Nonmetallic helical ultrasonic motors can be used to achieve 3D IVUS imaging in a strong magnetic field.

V. Conclusion

In this work, a novel 3D IVUS imaging method using a helical ultrasonic motor was proposed to explore the possibilities of the miniature 3D intravascular imaging system. A miniature helical ultrasonic motor was used to rotate and pullback the IVUS catheter to acquire 3D images visualizing the morphologies of artery vessels. The most significant advantage of the IVUS system is that the EMI-free ultrasonic motor is smaller, lighter, and more flexible than traditional EM motors, achieving better raw 3D images. The IVUS system could provide an axial resolution of 48 μm. Therefore, the layers within the porcine coronary artery, which closely matched those of human arteries, could be precisely identified. In conclusion, the proposed method provides a feasible technique for fabricating miniature 3D IVUS systems.

References

[1] G. A. Roth, et al., "Global, regional, and national burden of cardiovascular diseases for 10 causes, 1990-2015," *J. Am. Coll. Cardiol.*, vol. 70, no. 1, pp. 1-25, May. 2017.

[2] V. Fuster, "Global burden of cardiovascular disease: Time to implement feasible strategies and to monitor results," *J. Am. Coll. Cardiol.*, vol. 64, no. 5, pp. 520-522, Aug. 2014.

[3] C. L. de Korte, S. Fekkes, A. J. Nederveen, R. Manniesing, and H. R. H.
G. Hansen, "Review: mechanical characterization of carotid arteries and atherosclerotic plaques," *IEEE Trans. Ultrason. Ferroelectr. Freq. Control*, vol. 63, no. 10, pp. 1613-1623, Oct. 2016.

[4] G. A. Mensah, A. E. Moran, G. A. Roth, and J. Narula, "The global burden of cardiovascular diseases, 1990-2010," *Glob. Heart*, vol. 9, no. 1, pp. 183-184, Mar. 2014.

[5] L. E. Burke, et al., "Current science on consumer use of mobile health for cardiovascular disease prevention: a scientific statement from the American Heart Association," *Circulation*, vol. 132, no. 12, pp. 11571213, Aug. 2015.

[6] G. S. Mintz, et al., "American College of Cardiology clinical expert consensus document on standards for acquisition, measurement and reporting of intravascular ultrasound studies (IVUS). A report of the American College of Cardiology Task Force on Clinical Expert Consensus Documents," *J. Am. Coll. Cardiol.*, vol. 37, no. 5, pp. 1478-1492, Mar. 2001.

[7] J. Hong, et al., "A dual-mode imaging catheter for intravascular ultrasound application," *IEEE Trans. Med. Imaging*, vol. 38, no. 3, pp. 657-663, Mar. 2019.

[8] Z. Ding and M. H. Friedman, "Dynamics of human coronary arterial motion and its potential role in coronary atherogenesis," *J. Biomech. Eng.*, vol. 122, no. 5, pp. 488-492, Oct. 2000.

[9] P. H. Stone, et al., "Effect of endothelial shear stress on the progression of coronary artery disease, vascular remodeling, and in-stent restenosis in humans: In vivo 6-month follow-up study," *Circulation*, vol. 108, no. 4, pp. 438-444, Jul. 2003.

[10] A. Fenster et al., "Three-dimensional ultrasound imaging," *Phys. Med. Biol.*, vol. 46, no. 5, pp. 67-99, Nov. 2000.

[11] C. Shi, X. Luo, J. Guo, Z. Najdovski, T. Fukuda, and H. Ren, "Threedimensional intravascular reconstruction techniques based on intravascular ultrasound: A technical review," *IEEE J. Biomed. Health Inform.*, vol. 22, no. 3, pp. 806-817, May. 2018.

[12] D. Wildes, et al., "4-D ICE: A 2-D array transducer with integrated ASIC in a 10-Fr catheter for real-time 3-D intracardiac echocardiography," *IEEE Trans. Ultrason. Ferroelectr. Freq. Control*, vol. 63, no. 12, pp. 2159-2173, Dec. 2016.

[13] J. Peng, L. Ma, X. Li, H. Tang, Y. Li, and S. Chen, "A novel synchronous micro motor for intravascular ultrasound imaging," *IEEE Trans. Bio Med. Eng.*, vol. 66, no. 3, pp. 802-809, Mar. 2019.

[14] C. Peng, H. Wu, S. Kim, X. Dai, and X. Jiang, "Recent Advances in Transducers for Intravascular Ultrasound (IVUS) Imaging,".

[15] J. Ma, et al., "Design factors of intravascular dual frequency transducers for super-harmonic contrast imaging and acoustic angiography," *Phys. Med. Biol.*, vol. 60, no. 9, pp. 3441-3457, Apr. 2015.

[16] X. Li, T. Ma, J. Tian, P. Han, Q. Zhou, and K. K. Shung, "Micromachined PIN-PMN-PT crystal composite transducer for high-frequency intravascular ultrasound (IVUS) imaging," *IEEE Trans. Ultrason. Ferroelectr. Freq. Control*, vol. 61, no. 7, pp. 1171-1178, Jun. 2014.

[17] X. Li, et al., "Integrated IVUS-OCT imaging for atherosclerotic plaque characterization," *IEEE J. Sel. Top. Quantum Electron.*, vol. 20, no. 2, p. 7100108, Mar. 2014.

[18] J. Li, et al., "Integrated IVUS-OCT for real-time imaging of coronary atherosclerosis," *JACC Cardiovasc. Imaging*, vol. 7, no. 1, pp. 101-103, Jan. 2014.

[19] S. Brugaletta and M. Sabaté, "Assessment of plaque composition by intravascular ultrasound and near-infrared spectroscopy: From PROSPECT I to PROSPECT II," *Circ. J.*, vol. 78, no. 7, pp. 1531-1539, Jun. 2014.

[20] T. Dohi, et al., "The relationship among extent of lipid-rich plaque, lesion characteristics, and plaque progression/regression in patients with coronary artery disease: A serial near-infrared spectroscopy and intravascular ultrasound study," *Eur. Heart J. Cardiovasc. Imaging*, vol. 16, no. 1, pp. 81-87, Jan. 2015.

[21] Y. Li, et al., "High-speed intravascular spectroscopic photoacoustic imaging at 1000 A-lines per second with a 0.9-mm diameter catheter," *J. Biomed. Opt.*, vol. 20, no. 6, p. 065006, Jun. 2015.

[22] K. Jansen, et al., "Spectroscopic intravascular photoacoustic imaging of lipids in atherosclerosis," *J. Biomed. Opt.*, vol. 19, no. 2, p. 026006, Feb. 2014.

[23] D. Gorpas, et al., "Fluorescence lifetime imaging and intravascular ultrasound: Co-registration study using ex vivo human coronaries," *IEEE Trans. Med. Imaging*, vol. 34, no. 1, pp. 156-166, Jan. 2015.

[24] X. Bai, et al., "Intravascular optical-resolution photoacoustic tomography with a 1.1-mm diameter catheter," *PLoS One*, vol. 9, no. 3, p. e92463, Mar. 2014.

[25] S. P. Bhavnani et al., "A randomized trial of pocket-echocardiography integrated mobile health device assessments in modern structural heart disease clinics," *JACC Cardiovasc. Imaging*, vol. 11, no. 4, pp. 546-557, Apr. 2018.

[26] T. Sashida and T. Kenjo, "An introduction to ultrasonic motors," UK. Jericho, Oxford: Clarendon Press, 1993, pp. 17-22.

[27] S. E. Song, J. Tokuda, K. Tuncali, C. M. Tempany, E. Zhang, and N. Hata, "Development and preliminary evaluation of a motorized needle guide template for MRI-guided targeted prostate biopsy," *IEEE Trans. Bio Med. Eng.*, vol. 60, no. 11, pp. 3019-3027, Nov. 2013.

[28] M. A. Tavallaei, Y. Thakur, S. Haider, and M. Drangova, "A magnetic-resonance-imaging-compatible remote catheter navigation system," *IEEE Trans. Bio Med. Eng.*, vol. 60, no. 4, pp. 899-905, Apr. 2013.

[29] C. M. Esser, C. Parthiban, and M. R. Zinn, "Development of a parallel actuation approach for MR-compatible robotics," *IEEE ASME Trans. Mechatron.*, vol. 19, no. 3, pp. 904-915, May. 2013.

[30] B. Koc, S. Cagatay, and K. Uchino, "A piezoelectric motor using two orthogonal bending modes of a hollow cylinder," *IEEE Trans. Ultrason. Ferroelectr. Freq. Control*, vol. 49, no. 4, pp. 495-500, Apr. 2002.

[31] Y. Furukawa, N. Tagawa, T. Moriya, S. P. Xie, and M. Tanabe, "P1D-5 Development of an Ultrasonic Probe for Rotating-type IVUS Incorporated Coiled Stator USM (CS-USM)," *IEEE International Ultrasonics Symposium (IUS)*, Vancouver, Canadian, Oct. 2006, pp. 1301-1304.

[32] S. Chang, E. Murdock, Y. Mao, C. Flueraru, and J. Disano, "Stationary-fiber rotary probe with unobstructed 360 view for optical coherence tomography," *Opt. Lett.*, vol. 36, no. 22, pp. 4392-4394, Nov. 2011.

[33] C. Zhao, "Ultrasonic Motors Technologies and Applications," China. Beijing: Science Press, 2001, pp. 196-201.

[34] B. Wang et al., 2020, Nov., "A Miniature Rotary-linear Ultrasonic motor for Intravascular Ultrasound (IVUS) Imaging," Presented at the *2020 IEEE Int. Ultrason. Symp. (IUS)* [Online]. Available at: https://ieeexplore.ieee.org/abstract/document/9251619.

[35] P. Kaczkowski. (2016). "Bandwidth Sampling Data Acquisition With the Vantage System for High Frequency Transducers," Kirkland, WA, USA: Verasonics, White paper, pp. 1-5, [Online]. Available at: https://verasonics.com/wp content/uploads/2017/08/Bandwidth_Sampling_white_paper_July2017.pdf.

[36] M. Welvaert and Y. Rosseel, "On the definition of signal-to-noise ratio and contrast-to-noise ratio for fMRI data," *PLoS One*, vol. 8, no. 11, p. e77089, Nov. 2013.

[37] G. McGibney and M. R. Smith, "An unbiased signal-to- noise ratio measure for magnetic resonance images," *Med. Phys.*, vol. 20, no. 4, pp. 1077-1078, Jul. 1993.

[38] C. Zhao, "Ultrasonic Motors Technologies and Applications," China. Beijing: Science Press, 2001, pp. 179-183.

[39] J. M. Thijssen, G. Weijers, and C. L. Korte, "Objective performance testing and quality assurance of medical ultrasound equipment," *Ultrasound Med. Biol.*, vol. 33, no. 3, pp. 460-471, Mar. 2007.

[40] S. Hou, et al., "A Novel Distal Micromotor Based Side-looking Intravascular Ultrasound Transducer," *IEEE Trans. Ultrason. Ferroelectr. Freq. Control*, Accessed on: Sept., 22, 2021, DOI: 10.1109/TUFFC.2021.3114414, [Online].

[41] A. Kanada and T. Mashimo, "Design and experiments of flexible ultrasonic motor using a coil spring slider," *IEEE ASME Trans. Mechatron.*, vol. 25, no. 1, pp. 468-476, Dec. 2019.

[42] J. Hui, et al., "Real-time intravascular photoacoustic-ultrasound imaging of lipid-laden plaque in human coronary artery at 16 frames per second," *Sci. Rep.*, vol. 7, no. 1, p. 1417, May. 2017.

[43] Y. Kawase, et al., "Comparison of nonuniform rotational distortion between mechanical IVUS and OCT using a phantom model," *Ultrasound Med. Biol.*, vol. 33, no. 1, pp. 67-73, Jan. 2007.

[44] W. Kang, et al., "Motion artifacts associated with in vivo endoscopic OCT images of the esophagus," *Opt. Express*, vol. 19, no. 21, pp. 2072220735, Oct. 2011.

[45] J. Oh, M. D. Feldman, J. Kim, C. Condit, S. Emelianov, and T. E. Milner, "Detection of magnetic nanoparticles in tissue using magneto-motive ultrasound," *Nanotechnology*, vol. 17, no. 16, pp. 4183-4190, Aug. 2006.

Boquan Wang received the M.E. degree from the Guangzhou University, Guangzhou, China, in 2019. He is currently pursuing his Ph.D. in the State Key of Mechanics and Control of Mechanical Structures of the Nanjing University of Aeronautics and Astronautics, Nanjing, China. His research interests include high-frequency ultrasound imaging, photoacoustic imaging, and ultrasonic motors technologies and their applications.

Yulin Zhou received the M.S. degree of clinical medicine from the Jiangsu University, Zhenjiang, China in 2018. He has been working at the Urology Department, Jingling Hospital, Nanjing, China, since 2018. He is currently pursuing the Ph.D. in the Soochow University with a focus on the treatment of sarcomatoid renal cell carcinoma.

Yuchen Wang is currently pursuing the B.E. degree in aircraft design and engineering with Nanjing University of Aeronautics and Astronautics, Nanjing, China, with a focus on ultrasound image processing.

Xiaoniu Li received the B.S. degree in mechanical engineering from Linyi University, Linyi, China, the M.S. degree in instrument science and technology from Nanjing University of Aeronautics and Astronautics, Nanjing, China, and the Ph.D. degree in engineering mechanics from Nanjing University of Aeronautics and Astronautics, in 2009, 2013, and 2018, respectively. Currently, he is working as a Lecturer with the College of Aerospace Engineering of the Nanjing University of Aeronautics and Astronautics, Nanjing, China. His research interests include dynamic analysis, vibration control and the technology of ultrasonic motors.

Liyuan He received the B.E. in information engineering and M.E. degrees in navigation, guidance and control from Nanjing University of Aeronautics and Astronautics, Nanjing, China, in 2014 and 2017, respectively, where she is currently pursuing the Ph.D. degree in mechanical design and theory with a focus on high-frequency ultrasound imaging and imaging processing.

Zhiyi Wen received the M.S. degree in Mechanical Engineering from Liaoning University of Technology, Jinzhou, Liaoning, China, in 2020. He is currently pursuing the Ph.D. in Mechanical Engineering with Nanjing University of Aeronautics and Astronautics, Nanjing, Jiangsu, China, with a focus on piezoelectric drive and control and vibration utilization.

Teng Cao received the B.S. degree in mechanical design, manufacturing and automation from Zaozhuang University, Zaozhuang, China, in 2014, the M.S. degree in mechanical engineering from Nanchang Hangkong University, Nanchang, China, in 2018. Currently, he is a Ph.D. candidate at Nanjing University of Aeronautics and Astronautics, Nanjing, China, with a focus on piezoelectric actuator.

Lei Sun received his B.S. degree in electrical engineering from the University of Science and Technology of China, Hefei, China, in 1996, his M.S. degree in electrical engineering from the Chinese Academy of Sciences, Beijing, China, in 2000, and his Ph.D. degree in bioengineering from The Pennsylvania State University, University Park, PA, in 2004. He then conducted postdoctoral research at the University of Southern California. And joined the Hong Kong Polytechnic University in 2008. Dr. SUN's research interests include understanding the underlying mechanisms and possible translational strategies of ultrasound neuromodulation and brain stimulation, investigating the potentials of ultrasound bio-effects for cancer therapy and diabetes, and multimodality molecular imaging and theranostics.

Dawei Wu (M'14) received the B.S. degree from Shanghai Jiao Tong University, Shanghai, China, in 1999, the
M.S. degree from the University of Miami, Coral Gables, FL, USA, in 2004, and the Ph.D. degree from the University of Southern California, Los Angeles, CA,
USA, in 2009, all in biomedical engineering. He is currently working as a Professor with the State Key of Mechanics and Control of Mechanical Structures of the Nanjing University of Aeronautics and Astronautics, Nanjing, China. He has authored and coauthored more than 40 research papers. He is currently the Deputy Editor-in-Chief of the *Journal of Vibration, Measurement and Diagnosis*. His research interests include high frequency ultrasound and miniature ultrasonic devices technologies and their applications.